



Chinese Society of Aeronautics and Astronautics
& Beihang University

Chinese Journal of Aeronautics

cja@buaa.edu.cn
www.sciencedirect.com



Panel/full-span free-wake coupled method for unsteady aerodynamics of helicopter rotor blade

Tan Jianfeng, Wang Haowen *

School of Aerospace, Tsinghua University, Beijing 100084, China

Received 10 February 2012; revised 15 October 2012; accepted 23 December 2012

Available online 17 May 2013

KEYWORDS

Free wake method;
Helicopter rotor;
Rotor wake;
Unsteady aerodynamics;
Unsteady panel method

Abstract A full-span free-wake method is coupled with an unsteady panel method to accurately predict the unsteady aerodynamics of helicopter rotor blades in hover and forward flight. The unsteady potential-based panel method is used to consider aerodynamics of finite thickness multi-bladed rotors, and the full-span free-wake method is applied to simulating dynamics of rotor wake. These methods are tightly coupled through trailing-edge Kutta condition and by converting doublet-wake panels to full-span vortex filaments. A velocity-field integration technique is also adopted to overcome singularity problem during the interaction between the rotor wake and blades. Helicopter rotors including Caradonna–Tung, UH-60A, and AH-1G rotors, are simulated in hover and forward flight to validate the accuracy of this approach. The predicted aerodynamic loads of rotor blades agree well with available measured data and computational fluid dynamics (CFD) results, and the unsteady dynamics of rotor wake is also well simulated. Compared to CFD, the present method obtains accurate results more efficiently and is suitable to rotorcraft aeroelastic analysis.

© 2013 Production and hosting by Elsevier Ltd. on behalf of CSAA & BUAA.

1. Introduction

The flow field around a rotorcraft is extremely complex because it is dominated by vortices shedding from rotor blades. In hover and low-speed forward flight, the rotor wake remains in the vicinity of the operating rotor blades. The close interaction of the rotor wake with rotor blades has a strong effect on rotor blade airloads and rotor wake dynamics. Due to the

complexity of rotor wake, determining pressure and load distribution is of critical importance to accurately predict rotorcraft performance, stability, loads, and aeroacoustic.

Base on Navier–Stokes equations for primitive variables, computational fluid dynamics (CFD) has been used to simulate the rotor wake^{1–4} and has great potential to provide insights into complex aerodynamic processes. This approach can adequately predict unsteady aerodynamic loads of blades, and has been used in comprehensive rotorcraft analysis in recent years.^{5,6} However, CFD methods are susceptible to excessive numerical dissipation of vorticity and are rather computationally expensive.

The free-wake method, which represents the rotor wake with vortex filaments, is a powerful approach to simulating complex rotor wake.^{7–10} In general, aerodynamics of rotor blade in the free-wake method is represented by lifting-line or lifting-surface method; however, these methods cannot

* Corresponding author. Tel.: +86 10 62792661.

E-mail addresses: windtam2003@yahoo.com.cn (J. Tan), bobwang@mail.tsinghua.edu.cn (H. Wang).

Peer review under responsibility of Editorial Committee of CJA.



Production and hosting by Elsevier

consider the effect of airfoils which has significant influence on aerodynamics.

For their simple and accurate computations, unsteady panel methods^{11–14} have been widely used as an alternative to CFD, lifting-line, and lifting-surface methods to predict aerodynamic loads in rotorcraft applications. However, simulating distorted wake behavior for a panel is difficult because a singularity problem arises when wake panels are close to one another. Therefore, the panel method is usually coupled with other wake dynamic methods. A panel method was coupled with a free-wake method by replacing doublet-wake panels with vortex-ring wake filaments,¹⁵ however, variation of doublet strength distribution was prescribed over blade camber line, and it was difficult to account for the effect of airfoils. The doublet panels were then distributed on blade surface in unsteady time-marching free-wake method to predict blade vortex interaction (BVI) noise.¹⁶ Moreover, based on a novel boundary integral formulation, a direct panel method was coupled with a free-wake method to analyze the BVI.¹⁷

Although the free-wake method coupled with a panel method can predict blade airloads and rotor wake dynamics, an accurate and efficient prediction has yet to be fully achieved. Moreover, there is a numerical singularity problem when the rotor wake approaches blades in forward flight. Therefore, a full-span free-wake method is coupled with an unsteady panel method to accurately predict the unsteady aerodynamics of rotor blades in this study. The method is achieved through trailing-edge Kutta condition and by converting doublet-wake panels to full-span vortex filaments. The doublet panels are distributed on the blade and shed wake surface. The shed wake is connected to the blade panels through trailing-edge Kutta condition. The rotor wake is described by full-span vortex filaments shedding from the shed wake. A second-order time-stepping scheme is applied to predict wake convection. A viscous vortex core model is adopted to avoid numerical singularity problem in velocity calculation, and a velocity-field integration technique is also used to reduce numerical instability of wake and panels when the rotor wake approaches rotor blades in forward flight.

Numerical results are compared with experimental data and CFD results for helicopter rotors, such as Caradonna–Tung, UH-60A, and AH-1G rotors, in hover and forward flight to validate the accuracy of the present method.

2. Computational method

2.1. Unsteady panel method

The fluid surrounding rotorcraft is assumed to be inviscid, irrotational, and incompressible.^{12,14} Therefore, a velocity potential ϕ can be defined and the continuity equation in terms of ϕ in the inertial frame of reference becomes

$$\nabla^2 \phi = 0 \quad (1)$$

Eq. (1) does not include time derivatives, and the time dependency is introduced through boundary conditions. The boundary condition for body surface, which requires the velocity component normal to the body surface S_B be zero, can be expressed as

$$\frac{\partial \phi}{\partial n} - \mathbf{v}_B \cdot \mathbf{n} = 0 \quad (2)$$

where \mathbf{v}_B is the velocity of a point on body surface S_B and \mathbf{n} denotes the outward unit normal vector at this point. In general, \mathbf{v}_B includes all the contributions of blade's rigid motion, blade's structural deformation, and fuselage's motion in maneuvering flight for rotorcraft. An infinity boundary condition requires that the flow disturbance should diminish far away from the body owing to the body's motion through the fluid.

$$\lim_{r \rightarrow \infty} \nabla \phi = 0 \quad (3)$$

where \mathbf{r} is the position vector (x, y, z) . This condition is automatically fulfilled through Green's function.

Following Green's identity, we can construct a general solution to Eq. (1) by summing up the source σ and doublet μ distributions placed on the body surface S_B and wake surface S_w .

$$\begin{aligned} \phi(x, y, z, t) = & \frac{1}{4\pi} \int_{S_B} \mu \mathbf{n} \cdot \nabla \left(\frac{1}{r} \right) dS - \frac{1}{4\pi} \int_{S_B} \sigma \left(\frac{1}{r} \right) dS \\ & + \frac{1}{4\pi} \int_{S_w} \mu \mathbf{n} \cdot \nabla \left(\frac{1}{r} \right) dS \end{aligned} \quad (4)$$

2.2. Boundary condition

According to the Neumann boundary condition, the velocity potential jump on S_B is $-\sigma$, and the source strength is

$$-\sigma = \mathbf{n} \cdot \mathbf{v}_B \quad (5)$$

The potential inside the body (without internal singularities) will not change for an enclosed boundary (e.g., S_B); therefore, the internal potential is set to $\phi_{\text{int}} = 0$. By dividing the blade surface into N panels and wake surface into N_w panels, integration on the surfaces in Eq. (4) can be equivalently written as the superposition of integrations on panels that constitute those surfaces. A constant-strength rectilinear panel is adopted in current study. Thus, the boundary condition for body surface can be rewritten as

$$\sum_{k=1}^N \mu_k C_k + \sum_{l=1}^{N_w} \mu_l C_l + \sum_{k=1}^N \sigma_k B_k = 0 \quad (6)$$

where

$$\begin{aligned} C &= \frac{1}{4\pi} \int_{\text{body or wake panel}} \mathbf{n} \cdot \nabla \left(\frac{1}{r} \right) dS \\ B &= -\frac{1}{4\pi} \int_{\text{body panel}} \left(\frac{1}{r} \right) dS \end{aligned} \quad (7)$$

To define this problem uniquely, the wake doublets should be known or related to the unknown doublets on S_B . The wake doublets can be expressed in terms of the unknown surface doublet through the Kutta condition. Defining upper and lower trailing edge (TE) doublets μ_u and μ_l , respectively, the TE wake doublet μ_{tw} is given as

$$\mu_{\text{tw}} = \mu_u - \mu_l \quad (8)$$

Eq. (6) can then be expressed as

$$\sum_{k=1}^N \mu_k A_k = -\sum_{l=1}^{N_w} \mu_l C_l - \sum_{k=1}^N \sigma_k B_k \quad (9)$$

where A_k includes contributions of the body surface as well as wake surface, and A_k , B_k , and C_l can be solved by the analytic formulations of Hess and Smith¹⁸ for a constant strength of

potential distribution on each panel. If the k th panel is not at the TE, then $A_k = C_k$; if it is, then $A_k = C_k \pm C_{tw}$.

2.3. Panel pressure and force

Once the flowfield is determined, the pressure on the body surfaces can be computed by using the velocity potential and flow velocity through the unsteady Bernoulli equation:

$$\frac{\partial \phi}{\partial t} + \frac{1}{2} \mathbf{v}^2 + \frac{1}{\rho} p = \frac{1}{\rho} p_{\text{ref}} \quad (10)$$

where \mathbf{v} , p , and p_{ref} are the local fluid velocity, local pressure, far-field reference pressure, respectively.

The non-dimensionalized form of the pressure is given as

$$C_p = \frac{p - p_{\text{ref}}}{(1/2)\rho \mathbf{v}_{\text{ref}}^2} = 1 - \frac{\mathbf{v}^2}{\mathbf{v}_{\text{ref}}^2} - \frac{2}{\mathbf{v}_{\text{ref}}^2} \frac{\partial \phi}{\partial t} \quad (11)$$

where \mathbf{v}_{ref} is the reference velocity. The reference velocity \mathbf{v}_{ref} includes the flight velocity, induced velocity by fuselage's motion, blade's rigid motion, and blade's deformation.

The aerodynamic force on the panels can be computed as

$$\Delta \mathbf{F}_k = -C_{pk}(\rho \mathbf{v}_{\text{ref}}^2/2)_k \Delta S_k \mathbf{n}_k \quad (12)$$

where $\Delta \mathbf{F}_k$ is the aerodynamic load on the panel, ΔS_k the panel area, and \mathbf{n}_k the normal vector.

2.4. Time-step free-wake method

The solution of the blade-doublet distribution is related to rotor wake, which is simulated by the free-wake method⁸⁻¹⁰ in the present study.

The free-wake method is based on the assumption of an incompressible flow, with all of the vorticity in the rotor wake discretized into straight-line vortex filaments. A description of the vorticity field in the rotor wake is governed by the three-dimensional, incompressible, viscous flow Navier–Stokes equations, which can be expressed with velocity–vorticity $(\mathbf{u}, \boldsymbol{\omega})$ as

$$\frac{\partial \boldsymbol{\omega}}{\partial t} + \mathbf{u} \cdot \nabla \boldsymbol{\omega} = \nabla \mathbf{u} \cdot \boldsymbol{\omega} + \nu \nabla^2 \boldsymbol{\omega} \quad (13)$$

where ν is kinematic viscosity. The first term on right hand side is strain term, and the second term is diffusion term. In many practical problems, it can be justified that the viscous term has little effect on rotor flow field, and the vortex filaments will then move freely as material lines with constant circulation. In this case, Eq. (13) can be a simpler convection form

$$\frac{d\mathbf{r}}{dt} = \mathbf{V}(\mathbf{r}, t), \quad \mathbf{r}(t=0) = \mathbf{r}_0 \quad (14)$$

where \mathbf{r}_0 is the initial position vector, and \mathbf{V} is the local velocity field. Vector \mathbf{r} is a function of the age of the vortex filament ζ and blade azimuth ψ where filament was trailed into rotor wake. Therefore, Eq. (14) can be written as the partial differential equation.

$$\frac{\partial \mathbf{r}(\psi, \zeta)}{\partial \psi} + \frac{\partial \mathbf{r}(\psi, \zeta)}{\partial \zeta} = \frac{1}{\Omega} \mathbf{V}(\psi, \zeta) \quad (15)$$

where Ω is the rotor speed.

The right hand side of Eq. (15) is the total convected velocity of the filament, which includes all the contributions

of freestream, blades' sources and doublets, shed-wake panels, and full-span vortex filaments.

$$\mathbf{V} = \mathbf{V}_{\infty} + \mathbf{V}_{\text{body panel}} + \mathbf{V}_{\text{shedwake panel}} + \mathbf{V}_{\text{fullspan wake}} \quad (16)$$

where \mathbf{V}_{∞} is freestream velocity, $\mathbf{V}_{\text{body panel}}$, $\mathbf{V}_{\text{shedwake panel}}$, $\mathbf{V}_{\text{fullspan wake}}$ are velocity induced by blade panels, shed-wake panels, and full-span wake filaments, respectively.

The induced velocity of vortex filaments is calculated through the Biot–Savart law. Vatisas vortex model¹⁹ is adopted in velocity calculation to avoid the singularity problem when $\mathbf{r} \rightarrow 0$. Viscous effect can be integrated into vortex model and the growth of viscous core radius for vortex filaments can be modeled by²⁰

$$r_c(\zeta) = \sqrt{r_{c0}^2 + 4\alpha\delta\nu\zeta/\Omega} \quad (17)$$

where r_{c0} is the initial vortex core radius, α the Oseen constant equaling to 1.25643, δ the eddy viscosity parameter.

Eq. (15) is solved through finite differences to approximate the space and time derivatives. The displacements of the filaments are then found in a time-stepping manner through numerical integration of the governing equations. The second-order-accurate predictor–corrector scheme (PC2B scheme)^{8,10} is employed in the present approach.

2.5. Blade motion

The rotor wake and blade airloads are closely related to blade-flapping response. Therefore, the individual blade-flapping dynamics is solved simultaneously with the rotor wake dynamics. The flap equation is given by the equilibrium of moments about the flapping hinge, which include all the contributions of blade aerodynamics, fuselage's motion, and blade's rigid motion. The blade-flapping behavior can be expressed as a set of ordinary differential equations, and the blade-flapping response is determined through the fourth-order Runge–Kutta scheme in current work.¹⁰

2.6. Coupled method

In general, the shed wake and trailing wake can be represented by wake panels. However, the wake panels can be replaced with a vortex wake to overcome the singularity problem when wake panels are close to one another.¹⁵⁻¹⁷ Therefore, the doublet-wake surface is replaced by full-span vortex filaments to describe complex wake behavior, which provides a connection between the unsteady panel method and the free-wake method. The blade panels, shed wake panels, and full-span vortex filaments are shown in Fig. 1. Rotor blades are represented by panels, the shed wake is described by doublet-shed wake panels, and the rotor wake is indicated by the full-span vortex filaments which connect to the shed wake.

The doublet-wake panels can be replaced by vortex filaments, and the equivalence of doublet panel surface and vortex filament can be expressed as²¹

$$\mathbf{V}_{\text{wake}} = \nabla \phi = -\frac{\mu}{4\pi} \int_{S_w} \nabla \frac{z}{r^3} dS = \frac{\Gamma}{4\pi} \int_C \frac{d\mathbf{l} \times \mathbf{r}}{r^3} \quad (18)$$

where C denotes the curve bounding of the wake panel, and $\Gamma = \mu$ is the circulation strength of the vortex filament along C . The order of vortex filament is one less than that of the

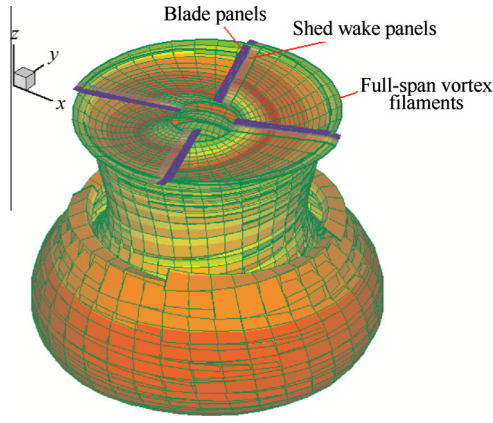


Fig. 1 Rotor wake system.

doublet panel, and the vortex filament is then less singular behavior than the doublet panel.

The strength of full-span vortex filaments is derived from the shed wake at each time step base on Eq. (18), which is shown in Fig. 2. The strength of the shed wake is obtained through the Kutta condition in Eq. (8). The strength of i th shed wake panel is μ'_i , and the next time step is $\mu'^{t+\Delta t}_i$, the strength of vortex filament parallel and perpendicular to the blade are then $\mu'^{t+\Delta t}_i - \mu'_i$, $\mu'_i - \mu'_{i+1}$, respectively.

The strength of the full-span vortex filaments is determined by blade panels, and the strength of doublet on blade panel is affected by the full-span vortex filaments at each time step, therefore, the full-span free-wake method is tightly coupled with the unsteady panel method.

2.7. Singularity problem

It is necessary to determine wake geometry before solving Eq. (9), and singularity problem in the numerical integration

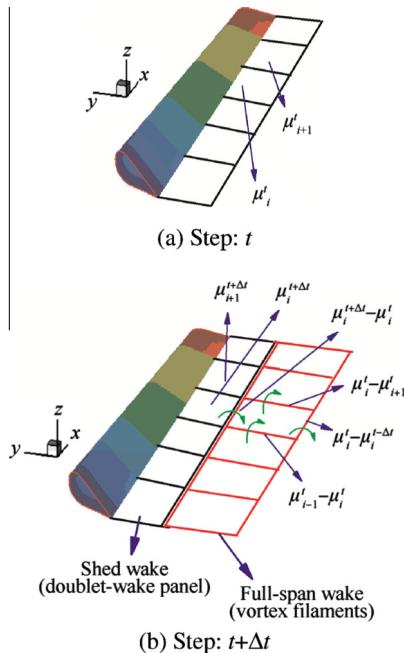


Fig. 2 Generation of full-span vortex filaments.

in Eq. (9) will occur when the rotor wake approaches blades on the advancing and retreating sides in forward flight (see Fig. 3).

A velocity-field integration technique^{17,22} is employed to overcome the singularity problem in the present study. The singularity problem is similar to that of velocity calculation; therefore, this problem can be avoided through that the wake potential is obtained indirectly by integrating the velocity field.

Velocity induced by wake vortex filaments can be expressed in Eq. (18), and the singularity can be overcome through Vatisas vortex model. The wake potential can be determined by integrating the velocity along an arbitrary integral path.

$$\phi_{\text{wake}} = \int_1^2 \left[\frac{\Gamma}{4\pi} \int_C G(\mathbf{r}) \frac{d\mathbf{l} \times \mathbf{r}}{r^3} \right] \cdot \mathbf{t}_p ds \quad (19)$$

where \mathbf{t}_p is the tangential vector of the integral path; the upper and down index 1, 2 are the initial point and ending point of integration, and G is Vatisas vortex model. This approach

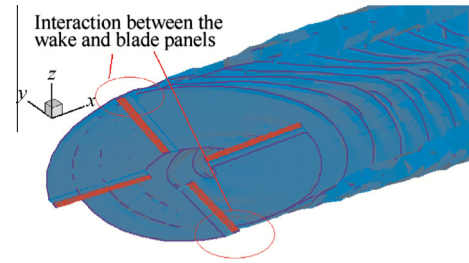


Fig. 3 Interaction between the wake and blade panels.

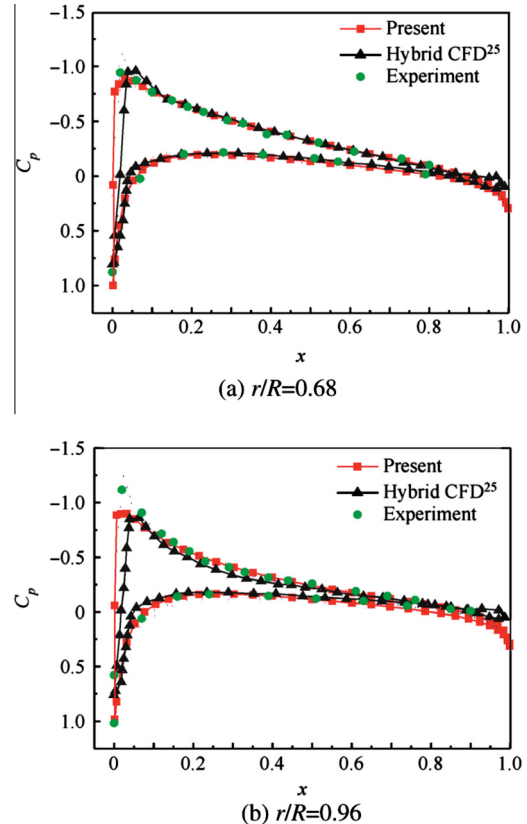


Fig. 4 Pressure coefficient over blade chord ($\Omega = 1250$ rpm).

prevents the numerical singularity problem which is very favorable to accurately predict pressure distribution when a BVI occurs in forward flight.

3. Numerical results and discussion

The blade pressure distribution and unsteady blade loads of the Caradonna–Tung, UH-60A, and AH-1G rotors are predicted and compared with available experimental data and CFD results to validate the proposed method.

3.1. Caradonna–Tung rotor in hover

Caradonna and Tung's²³ two-bladed rotor experiment is analyzed for a hovering rotor. This rotor has two untwisted, untapered, rectangular blades with NACA0012 airfoil. The rotor

radius is 1.143 m and the aspect ratio is 6. This case involved a rotor with a collective pitch angle of 8° , rotating at 1250, 1500, or 1750 rpm, corresponding to a tip Mach number of 0.439, 0.526, and 0.612, respectively.

The computational model was composed of 60 panels in the chordwise direction and 20 panels in the spanwise direction on each blade. The results for the current case were obtained with an azimuthal step of 10° and about 11 h with one CPU for 31 revolutions.

Figs. 4–6 show the pressure coefficient C_p at two blade-span sections ($r/R = 0.68, 0.96$, where r is radial distance, R is blade radius) with different tip Mach numbers. The experimental data,²³ CFD results,²⁴ and Hybrid CFD results²⁵ are shown for comparison. The CFD method²⁴ used multi-block structured mesh to account for blade's rigid motion through sliding-plane approach, and employed mesh-deformation technique to account for blade deflections through trans-finite interpolation (TFI) method. The Hybrid CFD method²⁵ included a compressible Navier–Stokes solver, a compressible potential flow solver, and a free wake model to accurately and efficiently predict unsteady blade pressure. The present numerical results are in fairly good agreement with the experimental results and the two different CFD results for all regions. However, the suction peak at the leading edge near the blade tip region is underestimated by the present and hybrid CFD results. Compared with CFD and hybrid CFD, the present method predicts aerodynamics of rotor blades in hover more efficiently.

3.2. UH-60A rotor in hover

The present method is also applied to the typical four-bladed UH-60A rotor.²⁶ This rotor has four complex blades with an

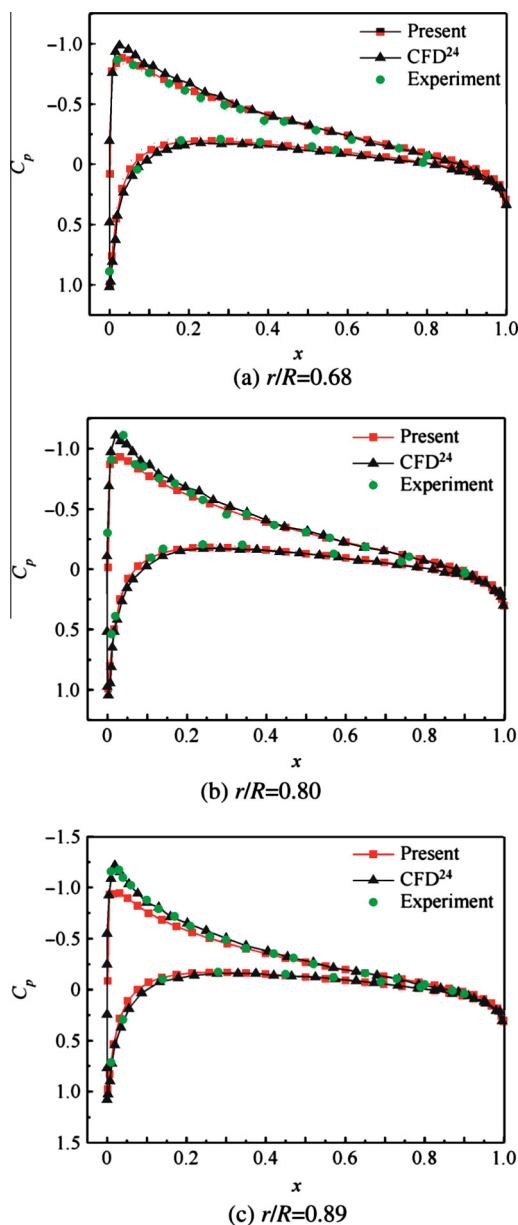


Fig. 5 Pressure coefficient over blade chord ($\Omega = 1500$ rpm).

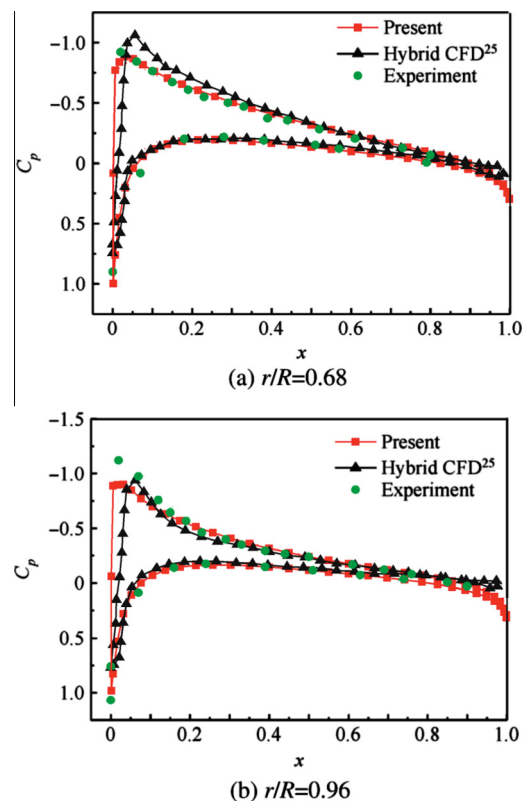


Fig. 6 Pressure coefficient over blade chord ($\Omega = 1750$ rpm).

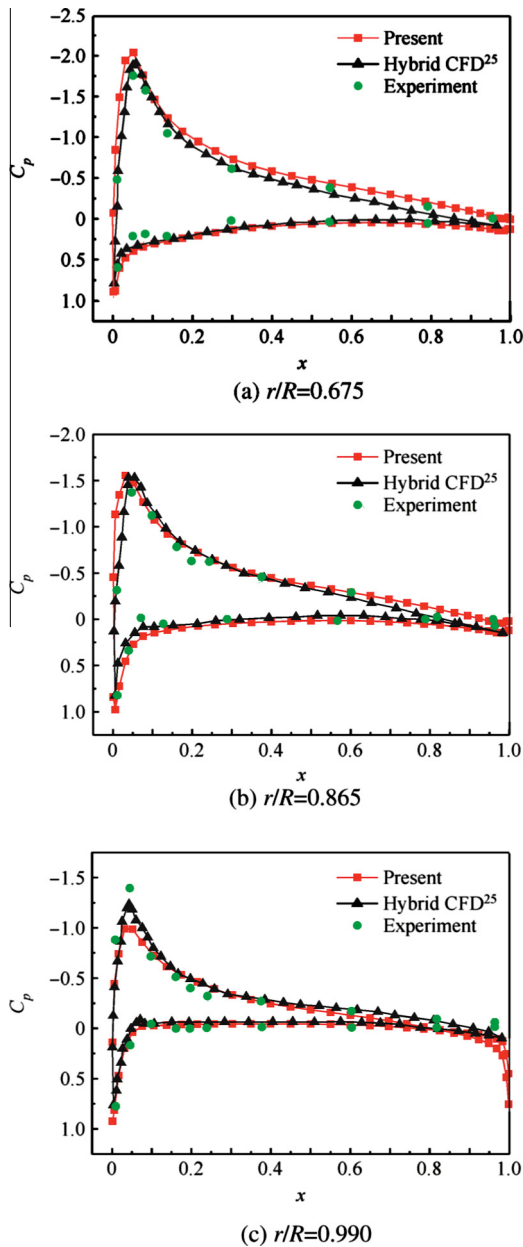


Fig. 7 Pressure coefficient over blade chord (UH-60A rotor).

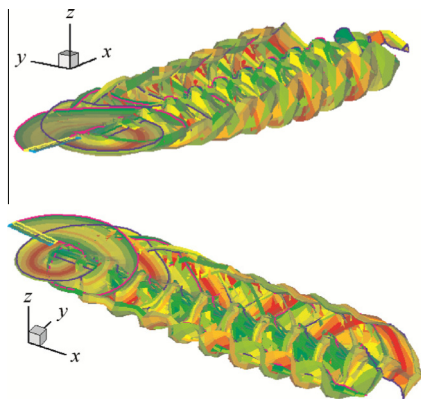


Fig. 8 AH-1G rotor wake geometry in forward flight.

aspect ratio of 15.3 and a maximum nonlinear twist of -13° . The blade has a rearward sweep of 20° starting from a rotor radius of 93% and is made up of two airfoil section, SC1095 as the main airfoil in inside and outside, and SC1095R8 section in the mid-span. The rotor is operated at a tip Mach number of 0.628 and with a collective pitch angle of 9° . The computational model is composed of 60 panels in the chordwise direction and 20 panels in the spanwise direction. An azimuthal step is 10° .

The rotor wake geometry is shown in Fig. 1. Wake contraction near the rotor plane and vortex bundle far below the plane is well captured. A comparison of the predicted pressure distribution at three radial stations ($r/R = 0.675, 0.865, 0.990$) with the corresponding experiment data and the hybrid CFD results²⁵ is shown in Fig. 7. The predicted results agree well with

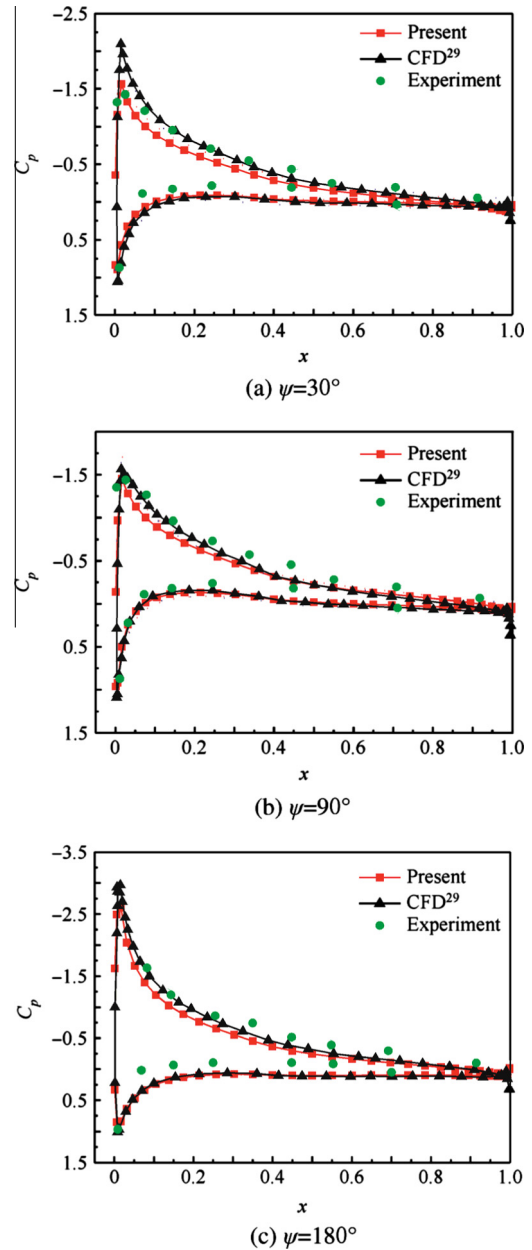


Fig. 9 Pressure coefficient at $r/R = 0.60$ (AH-1G).

the experimental data and the hybrid CFD results. At the station $r/R = 0.990$, the suction peak is underestimated by the present and hybrid CFD results. The pressure at trailing edge is overestimated by the present result, and one of the reasons is that the roll-up of shed wake described by doublet-wake panels is neglected in the present method, and this behavior will affect panels near trailing edge in tip region.

3.3. AH-1G rotor in forward flight

The AH-1G model^{27,28} in forward flight is also simulated. This rotor has two untapered, rectangular blades with OLS/TAAT airfoil. The rotor radius is 6.7 m and the aspect ratio is 9.2. The linear twist is -10° . The rotor is operated at a tip Mach number of 0.68 and an advance ratio of 0.19. The computational blade model was composed of 60 panels in the chordwise

direction and 20 panels in the spanwise direction. The results were obtained with an azimuthal step of 5° and about 24 h with one CPU for 10 revolutions.

The wake structure is shown in Fig. 8. The roll-up wake on the advancing and retreating side is captured well and wake convection is also observed. The wake in the forward part of the rotor is raised up towards the rotor disc, and the blade tip vortex approaches to the other blades, resulting in an interaction between the wake and blades. The singularity problem on the advancing side and retreating side is overcome.

Figs. 9 and 10 show the pressure coefficients at specific span positions ($r/R = 0.60, 0.91$) at azimuth angles of $30^\circ, 90^\circ, 180^\circ, 270^\circ, 285^\circ$, and 300° . The CFD results²⁹ are also shown for comparison. The predicted results agree well with measured data and CFD results at different azimuths. The suction peaks on the advancing side and retreating side are captured

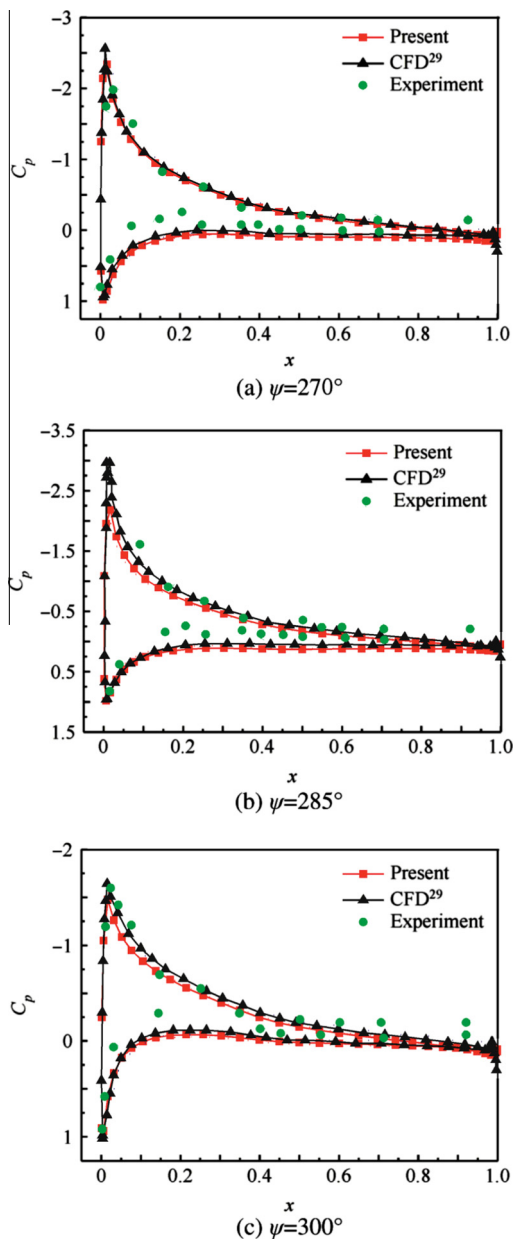


Fig. 10 Pressure coefficient at $r/R = 0.91$ (AH-1G).

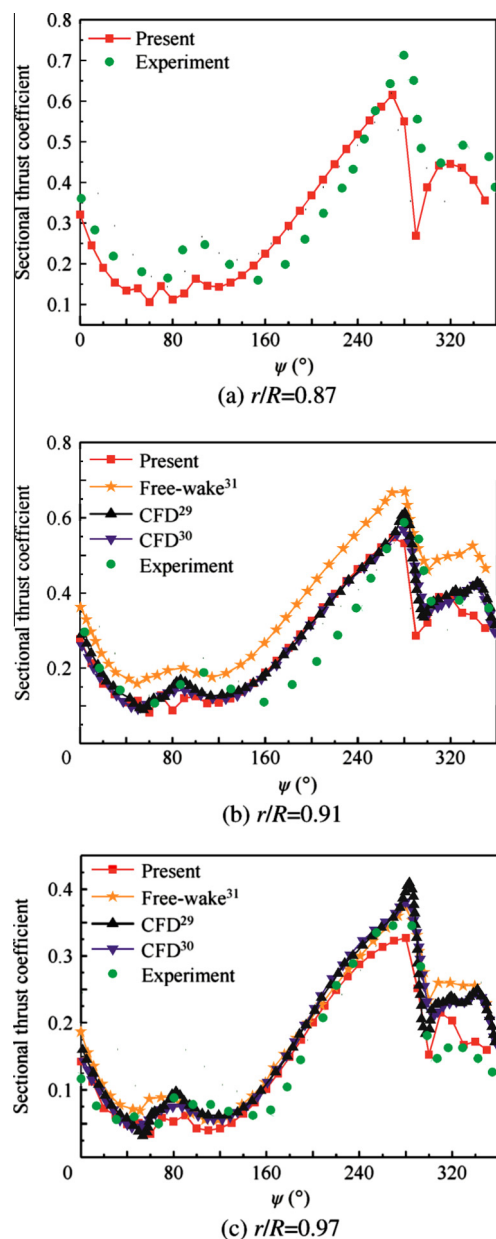


Fig. 11 Sectional thrust coefficients history (AH-1G).

fairly well with the CFD results; however, the suction peaks at azimuths of 270° are overestimated by both methods.

Fig. 11 shows the variation of the sectional thrust coefficient at the three blade radial stations over one revolution. The results are compared with measured data,^{27,28} CFD,^{29,30} and conventional free-wake results.³¹ The predicted unsteady thrust coefficients agree well with the flight test data and CFD results in different spans, and are more accurate than conventional free-wake results. The variations of the thrust coefficient correlate well with the measured data and CFD results near the azimuths of 90° and 270° . The influence of the interaction between the wake and blades on sectional thrust distributions is observed on the advancing side at azimuths of around 60° – 100° and on the retreating side at around 280° . Because the blade elastic deformation has impact on blade geometry, there is a discrepancy among the present, both CFD results, and the measured data from azimuthal angles of 180° – 280° .

The section oscillatory pitching moment coefficient (the mean value have been removed from the measured data and calculations) is shown in Fig. 12. The predicted results are compared with the measured data and CFD results.²⁹ The overall variation of oscillatory pitching moment agrees well with the measured data and CFD results; however, there are still discrepancies. One of the reasons is that there is discrepancy of pressure at leading edge and trailing edge, and the pressure distribution in chordwise direction has significant

impact on section pitching moment. Another reason is the influence of aeroelasticity which is neglected in present simulation.

The present method can accurately predict unsteady aerodynamic loads of rotor blades. Compared with CFD, this method is more efficient and suitable to rotorcraft aeroelastic analysis.

4. Conclusions

- (1) The blade pressure distribution predicted by the present unsteady panel/full-span free-wake coupled method is in a good agreement with measured data and CFD results in hover and forward flight for this article. The unsteady aerodynamic loads of blade agree fairly well with measured data and CFD results, and are more accurate than conventional free-wake results.
- (2) Wake contraction, convection, and roll-up behavior are captured well in hover and forward flight. The singularity problem of the interaction between the wake and blades is overcome.
- (3) The present method predicts unsteady aerodynamics of rotor blade more efficiently than CFD, and is suitable to rotorcraft aeroelastic analysis.

References

1. Markus D, Manuel K, Ewald K, Siegfried W. Tip vortex conservation on a helicopter main rotor using vortex-adapted chimera grids. *AIAA J* 2007;**45**(8):2062–74.
2. Steijl R, Barakos GN. Computational study of helicopter rotor-fuselage aerodynamic interactions. *AIAA J* 2009;**47**(9):2143–57.
3. Shi YJ, Zhao QJ, Fan F, Xu GH. A new single-blade based hybrid CFD method for hovering and forward-flight rotor computation. *Chin J Aeronaut* 2011;**24**(2):127–35.
4. Cao YH, Yu ZQ, Su Y, Kang K. Combined free wake/CFD methodology for prediction transonic rotor flow in hove. *Chin J Aeronaut* 2002;**15**(2):65–71.
5. Sitaraman J, Roget J. Prediction of helicopter maneuver loads using a fluid-structure analysis. *J Aircr* 2009;**46**(5):1770–84.
6. Mishra A, Ananthan S, Baeder JD. Coupled CFD/CSD prediction of the effects of trailing edge flaps on rotorcraft dynamic stall alleviation. In: *47th AIAA aerospace sciences meeting including the new horizons forum and aerospace exposition*, 2009. p. 1–17.
7. Bagai A, Leishman JG. Rotor free-wake modeling using a pseudo-implicit algorithm. *J Aircr* 1995;**32**(6):1276–85.
8. Bhagwat MJ, Leishman JG. Stability consistency and convergence of time-marching free-vortex rotor wake algorithms. *J Am Helicopter Soc* 2001;**46**(1):59–71.
9. Li CH, Xu GH. The rotor free-wake analytical method for tiltrotor aircraft in hover and forward flight. *ACTA Aerodyn Sin* 2005;**23**(2):152–156 [Chinese].
10. Tan JF. *Analysis of rotor aerodynamic response under manoeuvring conditions dissertation*. Nanjing: Nanjing University of Aeronautics and Astronautics; 2009 [Chinese].
11. Morino L, Kuo C. Subsonic potential aerodynamics for complex configuration. *AIAA J* 1974;**12**(2):191–7.
12. Katz J, Maskew B. Unsteady low-speed aerodynamic model for complete aircraft configurations. *J Aircr* 1988;**25**(4):302–10.
13. Morino L, Bharadvaj BK, Freedman MI, Tseng K. Boundary integral equation for wave equation with moving boundary and applications to compressible potential aerodynamics of airplanes and helicopter. *Comput Mech* 1989;**4**(4):231–43.

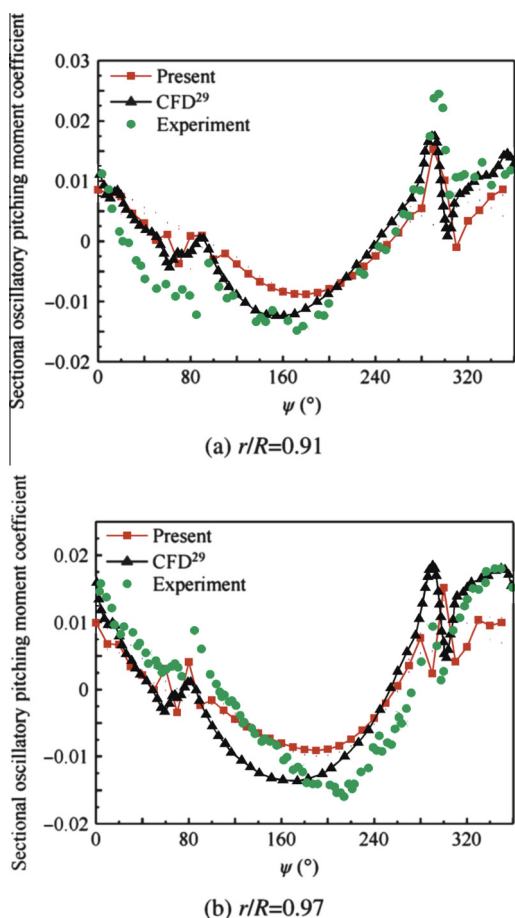


Fig. 12 Oscillatory pitching moment history (AH-1G).

14. Richason TF, Katz J. Unsteady panel method for flows with multiple bodies moving along various paths. *AIAA J* 1994;**32**(1):62–8.
15. Ahmed S, Vidjaja VT. Unsteady panel method calculation of pressure distribution on BO105 model rotor blades. *J Am Helicopter Soc* 1998;**43**(1):47–56.
16. Chung KH, Hwang CJ, Park YM, Jeon WJ, Lee DJ. Numerical predictions of rotorcraft unsteady air-loadings and BVI noise by using a time-marching free-wake and acoustic analogy. In: *31th European rotorcraft, forum*; 2005. p. 1–8.
17. Gennaretti M, Bernardini G. Novel boundary integral formulation for blade-vortex interaction aerodynamics of helicopter rotors. *AIAA J* 2007;**45**(6):1169–76.
18. Hess J, Smith AMO. Calculation of non-lifting potential flow about arbitrary three-dimensional bodies. *J Ship Res* 1964;**8**(2):22–44.
19. Vatistas GH, Kozel V, Mih WC. A simpler model for concentrated vortices. *Exp Fluids* 1991;**11**(1):73–6.
20. Bhagwat MJ, Leishman JG. Generalized viscous vortex model for application to free-vortex wake and aeroacoustic calculations. In: *The international 58th annual forum and technology display of the American Helicopter Society*; 2002. p. 11–3.
21. Morino L. Boundary integral equations in aerodynamics. *Appl Mech Rev* 1993;**46**(8):445–66.
22. Seong YW, Seongkyu L, Duck JL. Potential panel and time-marching free-wake coupling analysis for helicopter rotor. *J Aircr* 2009;**46**(3):1030–41.
23. Caradonna FX, Tung C. Experimental and analytical studies of a model helicopter rotor in hover. NASA TM-81232; 1982.
24. Steijl R, Barakos GN, Badcock KJ. A CFD framework for analysis of helicopter rotors. In: *17th AIAA computational fluid dynamics conference*; 2005. p. 1–14.
25. Berkman ME, Lakshmi NS, Charles RB, Michale ST. A Navier–Stokes/full potential/free wake method for rotor flows. AIAA-1997-401; 1997. p. 1–8.
26. Lorber PF, Stauter RC, Landgrebe AJ. A comprehensive hover test of the airloads and airflow of an extensively instrumented model helicopter rotor. In: *Proceedings of 45th annual forum of the AHS*, Boston; 1989.
27. Cross JL, Watts ME. Tip aerodynamics and acoustics test: a report and data survey. NASA-RP-1179; 1988.
28. Cross JL, Wilson T. Tabulation of data from the tip aerodynamics and acoustics test. NASA TM-102280; 1990.
29. Jee WK, Soo HP, Yung HY. Euler and Navier–Stokes simulations of helicopter rotor blade in forward flight using an overlapped grid solver. In: *19th AIAA computational, fluid dynamics*; 2009. p. 1–13.
30. Park YM, Kwon OJ. Simulation of unsteady rotor flow using unstructured adaptive sliding meshes. *J Am Helicopter Soc* 2004;**49**(4):391–400.
31. Joonbae L, Kwanjung Y, Sejong O. Development of an unsteady aerodynamic analysis module for rotor comprehensive analysis code. *J Aeronaut Space Sci* 2009;**10**(2):23–33.

Tan Jianfeng received the B.S. and M.S. degrees from Nanjing University of Aeronautics and Astronautics in 2007 and 2009 respectively, and then became a Ph.D. candidate in Tsinghua University. His main research interests are aerodynamics and overall design of helicopter.

Wang Haowen received the Ph.D. degree from Tsinghua University in 1998, and became a professor there since 2007. His main research interests are aeroelasticity and structure design of helicopter.